Making it big : how characean algae use cytoplasmic streaming to enhance transport in giant cells

Meent, J.W. van de

4 IMPLICATIONS FOR DIFFUSIVE TRANSPORT

In this chapter we aim to quantify in what ways the flow field in characean internodes can aid transport of nutrients and metabolites. Specifically, we would like to understand why the flowing bands in Chara are helically shaped. As we argued in chapters 1 and 2, streaming could benefit characean cells in a number of ways. One reason for streaming to exist is to facilitate transport between cells, another often expressed notion is that streaming benefits *homoeostasis* by enhancing mixing inside the cell. In the previous chapter we have seen that the helical nature of internodal flow implies the existence of a small transverse circulation whose magnitude is expected to be about 0.5% of the streaming velocity at the peak of cell development. In this chapter we will analyse how this circulation affects mixing and downstream transport in the vacuole.

We will begin by examining how the transverse circulation found in the last chapter could affect transport into and out of the vacuole. To do so we look at the transient re-equilibration of the vacuolar concentration after a jump at the boundary. We find that the presence of the transverse circulation leads to an asymmetrical concentration profile during re-equilibration. At the neutral line where flow is directed outward, vacuolar fluid is pushed into the wall, creating a boundary layer whose thickness decreases with the Péclet number. At the other neutral line, the saturated boundary layer is advected inward from the wall, forming a tongue shaped front. Together these effects help maintain higher concentration gradients near the cell periphery, thereby enhancing the flux across the boundary.

In the second part of this chapter, we explore the effect of the circulation on transport up and down the cell. Here, we approximate flow as purely advective, and look at the dispersion of a collection of trajectories over time. It is found the circulation homogenises the rate of transport along the z-axis by moving stationary particles in the centre of the cell towards faster moving regions in the periphery, leading to a smaller variability in the time-averaged rate of transport.

While both these effects suggest the cell may indeed be able to derive benefit from having a helically directed flow, a big question that remains difficult to answer is whether the strength of transverse circulation observed *in vivo* is strong enough to be significant. We therefore close the chapter with a re-examination of the growth data by Green (1954) to better assess the magnitude of the effects that could be observed *in vivo*.

4.1 Radial Mixing in the Vacuole

Characean internodes undergo an extraordinary expansion of cellular volume during development, growing from tens of micrometers to several centimetres in the space of a few days. As discussed in the previous chapter, radial diffusion could be a rate-limiting process during this phase of rapid growth. So one purpose of the transverse circulation in rotational streaming may be to enhance the flow of metabolites from the vacuolar bulk to the cytoplasm during development.

As discussed in the previous chapter, the strength of the transverse component of flow is parametrised by a dimensionless amplitude α_ψ that attains a maximum of 0.074 at $\lambda = 2.8$. The range of wavelenghts found in vivo is something like $10 - 80$. The work by Green (1954) indicates that the helical twist in the cells typically increases initially, peaking at a wavelength $\lambda \simeq 9$ in the middle of cell development when exponential growth is largest. At this wavelength, the amplitude α_ψ is about 0.008. If we define the Péclet number of the transverse circulation as $\mathrm{Pe}^* = \alpha_\psi \mathrm{Pe}$, we see that at in this phase of development Pe^* will be order one at moderate Péclet numbers just over 100. At this early stage of development, the cell radius tends to be smaller than that of a mature cell. But even in a cell with a relatively small radius of 200 μm typical time scales $T_D = R^2/D$ for diffusion are macroscopic, ranging from about a minute for a small molecule like an amino acid ($D = 700\ \mu\mathrm{m}^2/\mathrm{s}$, Polson (1937)), to roughly an hour for a protein with a diffusion constant of $10\ \mu\mathrm{m}^2/\mathrm{s}$. Given these long time scales, even a moderate enhancement of vacuolar mixing could be significant. Assuming a streaming rate of $V = 60$ μm/s, the Péclet number $\mathrm{Pe} = VR/D$ associated with these diffusion constants lies in the range $17 - 1000$, indicating the transverse Péclet number Pe^* would lie somewhere in the range $0.10 - 10$. Any enhancement of mixing and transport could therefore be an order one effect.

To obtain a measure of the influence of circulation on transport from vacuole to cytoplasm, we will attempt to construct a basic model that contains all the physics of the problem. We will assume that the vacuole contains a solute of concentration ρ_0, that is well-mixed at $t = 0$. We will then calculate the response to a jump in concentration at the boundary. In a sense this problem is the simplest parameter-free method of quantifying the influence of streaming on diffusive transport in the cell.

The evolution of a solute in the presence of a flow field is described by

the advection-diffusion equation (3.12)

$$\partial_t \rho + \mathrm{Pe}(\boldsymbol{u} \cdot \nabla)\rho = \nabla^2 \rho, \qquad \mathrm{Pe} = VR/D.$$

The choice of boundary conditions in this problem has the advantage that there is no depenedence on the φ or H coordinates in the initial condition. Since the flow field is symmetrical along H the advection-diffusion problem will retain this symmetry, simplifying the equations that need to be solved to a two-dimensional form in r and φ. This equation is also entirely linear, so we can rescale ρ by an arbitrary factor. Since any constant concentration ρ_0 is also a solution, we can subtract out the initial concentration and rescale the concentration jump to 1 without loss of generality.

It therefore suffices to look at the normalised problem, where the initial concentration $\rho = 0$ throughout the vacuole at $t = 0$ and $\rho(t, 1, \varphi) = 1$ at the boundary. Given this definition, our problem now describes flux into the vacuole after an increase in concentration at the boundary. In a mathematical sense this problem is of course identical to a flux out of the vacuole after a decrease in concentration at the periphery, since this reversal of the direction of flux is equivalent to a multiplication of the equations by a factor −1.

4.1.1 Numerical Integration of the Advection Diffusion Equation

The equation above is well known and a numerical solution may be obtained in a variety of ways. Since the solution of the flow field is calculated in terms of a Fourier decomposition, we will do the same for the density field, calculating a set of radial density modes of the form

$$\rho(t, r, \varphi) = \sum_n \rho^n(t, r) \cos(n\varphi) \,. \tag{4.1}$$

As with the flow field, it proves most convenient to solve this equation in cylindrical coordinates. The advection diffusion equation for this particular flow problem preserves the symmetry of the initial condition in the sense that an initial condition which is even in φ will produce a solution that is even in φ for all t. Since our $\rho = 0$ initial condition is indeed even, the problem is fully described by a $\cos(n\varphi)$ series and no $\sin(n\varphi)$ modes need to be considered.

The equations for the radial modes $\rho^n(t, r)$ are a set of PDE's in t and r. We discretise these equations by using a standard finite difference scheme

with four-point approximations for the derivatives in r. This produces a set of ODE's in t that we integrate using the Fortran-based LSODE solver (Hindmarsh, 1983).

The results presented below are based on two sets solutions. For the first set, we calculated the transients for a range of wavelengths

$$\lambda = 3.0, 5.7, 12.0, 25.0, 47.0 \ ,$$

and a range of Péclet numbers

$$\begin{aligned} \mathrm{Pe} = {} & 0, 1, 10, 20, 50, 100, 200, 500, \\ & 1\,000, 2\,000, 5\,000, 10\,000, 20\,000, 50\,000 \ . \end{aligned}$$

A set of 24 modes was calculated and 100 radial grid points were used for each mode. The flow field was solved using the tanh smoothed boundary condition described in the previous chapter (eq. 3.23), with cross-over width $\varepsilon = \pi/32$.

Since the shape of the flow field presented in chapter 3 shows only a weak dependence on the helical wavelength, we expect the response in the concentration field to be largely determined by the strength of the transverse component, which is parametrised by $\mathrm{Pe}^* = \alpha_\psi \mathrm{Pe}$. We therefore calculate a second set of high resolution solutions at $\lambda = 3.0$, which loosely corresponds to the wavelength that maximises the strength of the transverse component. Here 32 modes were integrated using 200 radial grid points for each mode. All other parameters were the same as for the first set. We will use these solutions for most of our analysis, with the first set serving as a check that the wavelength dependence can effectively be scaled out using a_ψ.

4.1.2 Response Time and Boundary Layer Scaling

Figures 4.1 and 4.2 show plots of the concentration during re-equilibration for Pe = 50 - 2 000, at a characteristic response time $t = \tau$ that will be defined below. The wavelength in these calculations is $\lambda = 3.0$, corresponding to a circulation amplitude of about 0.073, so the transverse Péclet number in these plots is $\mathrm{Pe}^* = 3.7 - 150$.

We see that the transverse asymmetry of the flow field is reflected in an increasingly well-defined asymmetry in the concentration profile. In the absence of flow (i.e. Pe = 0), uptake is diffusion-limited and a symmetric saturation layer develops at the boundary of the vacuole. The effect of the

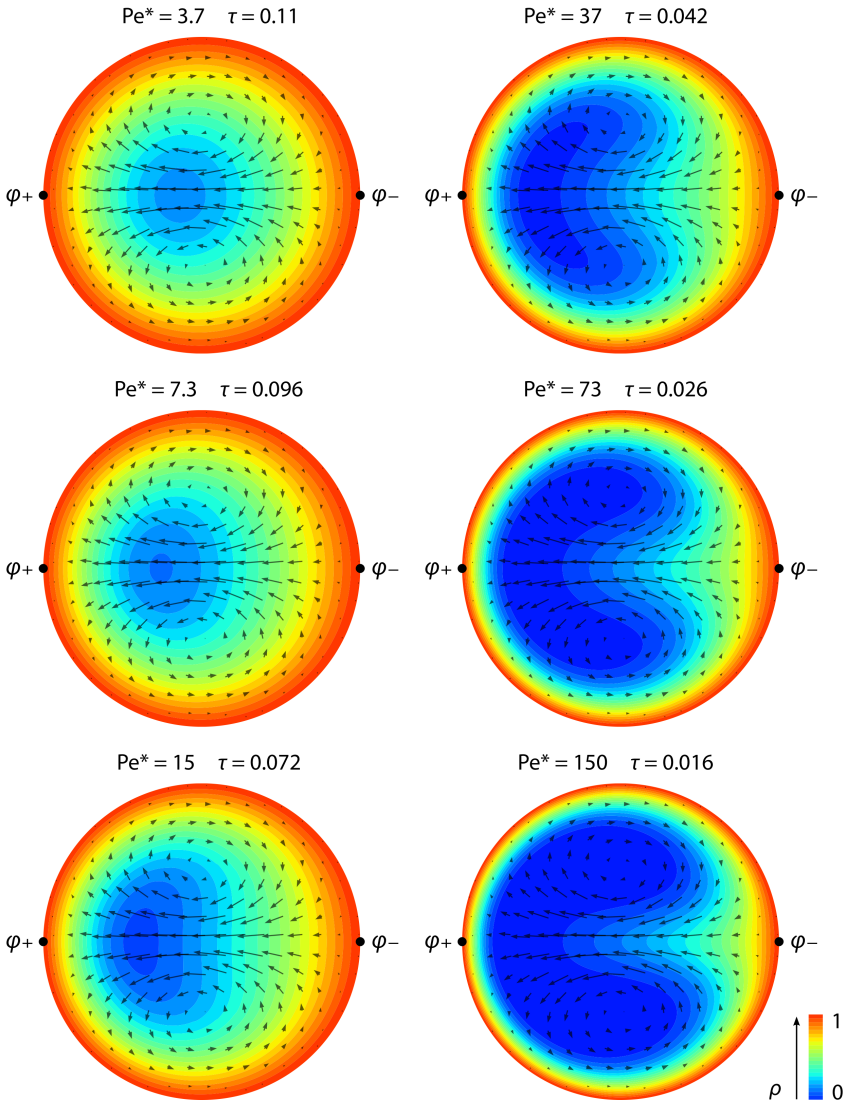

Figure 4.1 Snapshots of the concentration field during transient response to a jump at the boundary for Pe = 50 − 2 000 and $\lambda = 3$. The plotted times $t = \tau$ correspond to the maximum of the concentration transient $\partial_t \rho$ at the centre of the cell. In the absence of advection the profile is symmetric. As Pe increases, a boundary layer develops at the *centrifugal* zone φ_+, where the outward flow maintains a region of high flux. At the *centripetal* zone φ_- a tongue-shaped front develops as pile-up is advected inward.

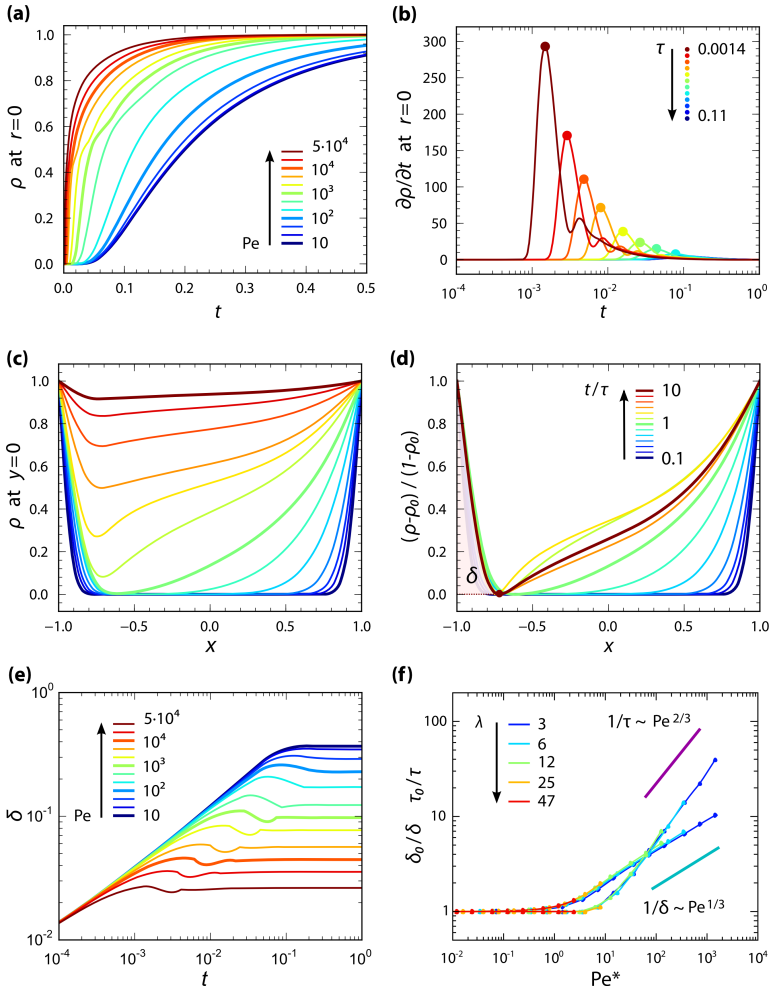

Figure 4.2 Dependence of re-equilibration transients on the Péclet number. **(a)** Concentration at $\rho = 0$. **(b)** A characteristic *response time* τ can be determined from the point in time where $\partial_t \rho$ peaks. **(c)** A set of concentration profiles along $y = 0$ for times $t = 0.1\tau$-10τ. **(d)** Renormalisation of the concentration using the concentration base level $\rho_0 = \min_x(\rho)$ reveals convergence to a time-independent profile. The area under the curve left of the minimum is used to define a *boundary layer* size δ. **(e)** The time-evolution of δ shows a clear Péclet dependence, implying an enhanced flux at the boundary due to an increase of the typical gradient. **(f)** Enhancement of boundary layer gradient and response time. $1/\tau$ and $1/\delta$ are normalised by their Pe = 0 values τ_0 and δ_0. The boundary layer size shows a $\mathrm{Pe}^{-1/3}$ scaling, whereas the response time scales as $\mathrm{Pe}^{-2/3}$. Curves for varying λ collapse when plotted as a function of $\mathrm{Pe}^* = \alpha_\psi \mathrm{Pe}$, indicating the magnitude of the transverse circulation parametrises the problem.

circulation is to redistribute low concentration material from the centre of the cell towards the periphery, and pull material from the saturated layer towards the centre of the cell.

One fundamental implication of this result is that the two neutral lines are no longer metabolically equivalent for a finite helical pitch. At the left-most neutral line, where flow is directed outward from the centre, this leads to the formation of a *boundary layer* that decreases in thickness as the Péclet number becomes larger. On the other side, a tongue shaped front is formed as material is advected inward. The combined result of these two effects is that a sharper concentration gradient at the boundary is maintained during uptake, thereby increasing the flux into the vacuole. To distinguish between the two neutral lines, we will from here onward use the term *centrifugal zone* (φ_+) to denote the region around the neutral line where flow is directed outward, and the term *centripetal zone* (φ_-) to denote the inward flowing zone.

In order to obtain a measure of the response time, we plot the time-dependence of the concentration at $r = 0$ and $\lambda = 3.0$ for increasing Péclet numbers. The resulting figure (4.2a) shows a very clear increase in the rate of change of the concentration as the Péclet number increases. A plot of the time derivative $\partial_t \rho(t, r, \varphi)$ at $r = 0$ (fig 4.2b) reveals that the flux into the centre has a well-defined peak, whose position shifts towards lower t showing a variation of two orders of magnitude as Pe is increases from 0 to 50 000. The position of this peak can be used to define a typical time τ that specifies the delay between the jump in concentration at the boundary and the response at the centre of the cell. It is these times that were chosen for the snapshots in figure 4.1.

Figure 4.2c shows the concentration along the $y = 0$ centre-line of the cell at a range of times at Pe $= 1000$. We see that the propagation of the tongue results in an increasingly asymmetric concentration profile. At $t \simeq \tau$ the tongue reaches the other side of the cell and the profile appears to retain a self-similar shape as the minimum concentration increases. Figure 4.2d shows the same profiles, this time renormalised by taking $(\rho - \min_x \rho)/(1 - \min_x \rho)$. We see that the normalised profile converges towards a well-defined asymptotic shape, which defines a typical length scale for the boundary layer size δ. We will define the size of this boundary layer as the surface area under the profile at the centrifugal side of the minimum:

$$\delta = \int_{-1}^{x_{\min}} \frac{\rho - \min_x \rho}{1 - \min_x \rho}\, dx$$

This length is roughly equivalent to the distance from the wall for which $\rho_{1x} = 0.5$. The above definition has the advantage that it is more computationally robust at high Pe, since it does not require interpolation of the curve near the wall.

In figure 4.2e we show the evolution of the boundary layer size with time. The initial growth of the boundary layer appears more or less independent of the Péclet number, indicating that fluxes are purely diffusive, while the asymptotic values decrease by roughly an order of magnitude as Pe increases from 0 to 50 000.

The dependence of δ and τ on Pe^* is shown in figure 4.2f. We observe a very clear scaling of both quantities with the Péclet number. The boundary layer size appears to show a $\mathrm{Pe}^{-1/3}$ dependence, whereas the response time scales as $\mathrm{Pe}^{-2/3}$. This scaling collapses across the range of wavelengths $\lambda = 3.0, 5.7, 12.0, 25.0, 47.0$, showing that Pe^* indeed parametrises the problem.

The decrease of the boundary layer size with the Péclet number can be understood through a standard dominant balance argument. In the vicinity of the indifferent zone, we can define a local set of Cartesian coordinates (x_1, x_2, x_3) that are the local linearised approximations of $(1-r, \varphi-\varphi_\pm, H)$. Thus, x_1 denotes the distance from the wall, x_2 the distance from the indifferent zone parallel to the wall, and x_3 the coordinate along the direction of flow. Since the problem is symmetrical along H, it will also be symmetrical along x_3 and the boundary, and only the (x_1, x_2)-dependence of the problem needs to be considered.

We can derive the lowest order expressions for the (u_1, u_2) components of flow from the symmetry of the stagnation point. At the $x_2 = 0$ centre-line, the u_2 component of flow must vanish. Moreover, u_2 must also be zero at the wall ($x_1 = 0$). Thus, to lowest order the component of flow parallel to the wall must scale as $u_2 \sim x_1 x_2$, since the flow is directed away from the centre line at the centrifugal zone. From the continuity condition $\partial_1 u_1 + \partial_2 u_2$, we then obtain

$$u_1 \simeq -\tfrac{1}{2} x_1^2 \,, \qquad\qquad u_2 \simeq x_1 x_2 \,. \tag{4.2}$$

If a boundary layer is to have a stable size, then locally

$$\partial_t \rho = -\boldsymbol{u} \cdot \nabla \rho + \frac{1}{\mathrm{Pe}^*} \nabla^2 \rho = 0 \,. \tag{4.3}$$

Using the lowest order approximation for the flow field above, this condi-

tion expands to

$$-\tfrac{1}{2}x_1^2\nabla_1\rho + x_1x_2\nabla_2\rho = \frac{1}{\mathrm{Pe}^*}(\nabla_1^2 + \nabla_2^2)\rho \ . \tag{4.4}$$

Now note that $\tilde{\nabla}_2\rho = 0$ since the concentration is symmetric around the indifferent zone. Moreover $\tilde{\nabla}_2^2\rho \ll \tilde{\nabla}_2^1\rho$ since the concentration is not narrowly peaked around the indifferent zone. We can therefore neglect the derivatives along the x_2 axis, reducing equation 4.4 to

$$-\tfrac{1}{2}x_1^2\nabla_1\rho = \frac{1}{\mathrm{Pe}^*}\nabla_1^2\rho \ . \tag{4.5}$$

If we now rescale x_1 coordinate by the boundary layer length δ, the above form becomes

$$-\frac{1}{2}\delta\tilde{x}_1^2\tilde{\nabla}_1\rho = \frac{1}{\mathrm{Pe}^*\,\delta^2}\tilde{\nabla}_1^2\rho \ . \tag{4.6}$$

In this rescaled form, both the coordinates and derivatives are order one, so if the advective term is to balance out the diffusive term, the scaling for the boundary layer should satisfy the condition

$$\delta^3 \sim \frac{1}{\mathrm{Pe}^*} \quad \rightarrow \quad \delta \sim \mathrm{Pe}^{*-1/3} \tag{4.7}$$

The $\mathrm{Pe}^{*-1/3}$ scaling observed in our solved profiles is therefore precisely the scaling expected for a boundary layer near a stagnation point of this topology.

The scaling of the response time can be understood by way of a similar argument. At the centripetal indifferent zone a boundary layer of increasing width is formed as the propagating front develops. On small time scales, the centripetal flux will be diffusion limited, since the advective field vanishes near the wall. At large time scales advection will dominate since $\mathrm{Pe}^* > 1$. The cross-over between these two regimes is at the point where the advective flux becomes equal to the diffusive flux, which is precisely when the centripetal front reaches the typical boundary layer size δ.

We can calculate this time scale by way of the following argument. As the boundary layer develops, the rate-of-change of ρ must be balanced by the total flux into the cell. Since the flux at the wall is given by $\partial_r\rho$, this yields the integral relation

$$\frac{d}{dt}\int \rho \, dr \, d\theta = \int \frac{\partial\rho}{\partial r} \, d\theta \ . \tag{4.8}$$

At small times, $\rho = 0$ everywhere, except near in a thin boundary layer near the periphery, whilst the gradient near the wall should scale as $1/\delta$. The above terms can therefore be approximated by

$$\int \rho \, dr \, d\theta \sim 2\pi\delta \,, \qquad \int \frac{\partial \rho}{\partial r} \, d\theta \sim 2\pi/\delta \,. \tag{4.9}$$

The evolution of the mean boundary layer size will therefore satifsy

$$\frac{d\delta}{dt} = \frac{1}{\delta} \quad \rightarrow \quad \delta \sim \sqrt{t} \tag{4.10}$$

as should be the case since the flux is diffusive on small time scales. Thus quite simply, the time required for formation of a typical boundary layer $\delta \sim \mathrm{Pe}^{*-1/3}$ scales as $\mathrm{Pe}^{*-2/3}$. In the asymptotic regime $\mathrm{Pe}^* \gg 1$ the time for boundary layer formation dominates over the time for advection into the centre, the response time τ is thus dominated by this scaling.

4.1.3 Eigenmode Bifurcation

While our time-scale τ provides and indication of when the response to a change in concentration becomes visible at the centre, it is not really a measure of the typical time for re-equilibration. If the peaks in flux in figure 4.2b were fully symmetrical in time, this point would correspond to the time at which $\rho = 0.5$ at $r = 0$. However, while the position of the maximum shifts inward with a $\mathrm{Pe}^{-2/3}$ scaling (4.2f), the decay of the curves in figure 4.5 shows a long tail in the flux after the peak. So whilst this point can be taken as a definition of the time at which the front propagating from the right indifferent zone reaches the centre, the value for ρ at $t = \tau$ and $r = 0$ in fact decreases with the Péclet number. Moreover since the width of the boundary layer decreases as well, mean concentration in the vacuole also decreases with Pe.

A better interpretation of τ is that it is an indication of the time at which deviations from diffusive behaviour set in. Figure 4.3a shows the standard deviation $\sigma(\rho)$ of the concentration field as a function of time, which is a measure of the degree of homogeneity. Since the system is homogeneous at $t = 0$ there is an initial diffusive growth, after which the standard deviation peaks and decays. The response time values is marked with circles on each plot. We see that τ roughly indicates the point in time where the curve starts to deviate from diffusive behaviour, which is to be

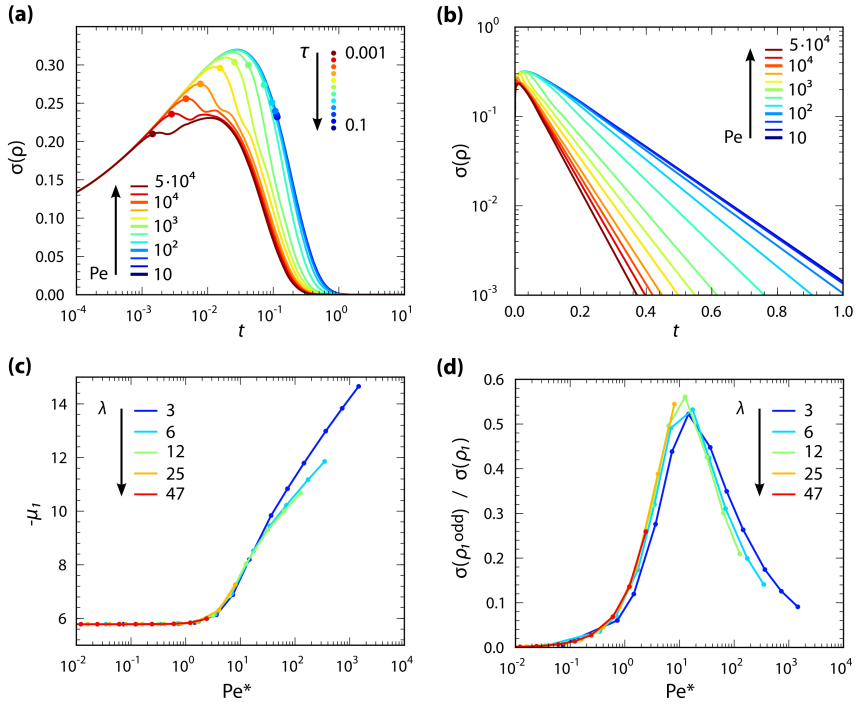

Figure 4.3 Decay of the slowest eigenmode ρ_1. **(a)** The spatially averaged standard deviation $\sigma(\rho)$ initially grows as the boundary layer develops and then decays as the system re-equilibrates. The response time τ roughly marks the point where deviations from the diffusive curve become significant. **(b)** The exponential tail of the $\sigma(\rho)$ decay is the signature of a slowest decaying mode $\rho_1 \exp(\mu_1 t)$. **(c)** The rate of decay $-\mu_1$ increases with the Péclet number, reflecting the enhanced flux due to sharper concentration gradients. **(d)** The asymmetry in the ρ_1 mode can be quantified by the relative magnitude of the odd terms in the expansion for the concentration field $\rho^n \cos(n\varphi)$. The slowest decaying eigenmode undergoes a form of bifurcation around $\mathrm{Pe}^* = 10$, approaching the symmetric diffusive profile at low Pe^* and a stream-function dominated profile at high Pe^*.

expected since this τ is roughly the time scale on which advective effects become stronger than diffusive effects.

In order to obtain a measure of the time for re-equilibration, we look at the decay of $\sigma(\rho)$ towards zero. In figure 4.3b the data is replotted on a logarithmic y-axis to show the tails of the curves. The linear tails reveal an exponential dependence on time. The decay rate appears more or less constant at low Pe^*, increases strongly at intermediate values and shows a

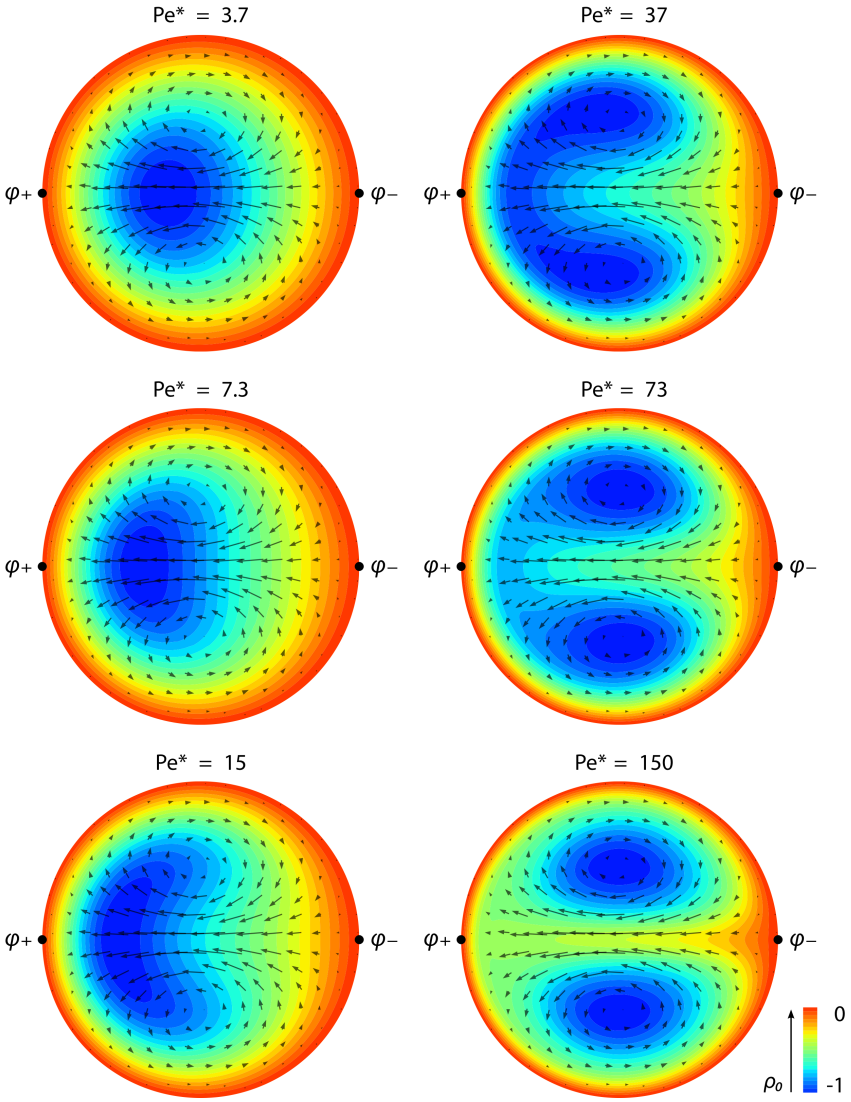

Figure 4.4 Slowest decaying eigenmodes ρ_1 for $\mathrm{Pe}^* = 3.7 - 150$. As Pe^* increases the minimum in the concentration profile shifts towards the centrifugal zone at φ_+. Around $\mathrm{Pe}^* = 15$ a form of bifurcation in the profile shape is visible. The single minimum near φ_+ splits into two minima at the centre of each circulation loop. We thus observe the strongest dependence on the Péclet number over the range $\mathrm{Pe}^* = 1 - 100$, with the ρ_1 mode converging to low Pe^* and high Pe^* asymptotic shapes further outward.

weak dependence at high Pe^* values. Looking at figure 4.3a we see a similar trend. The curves at low Pe^* essentially fall on top of each other, after which a shift occurs, whilst the curves for $\mathrm{Pe}^* > 100$ appear to converge again. For the four highest Pe^* values in particular we see that whilst the standard deviation starts to differ from the purely diffusive behaviour at $t = \tau$, the decay subsequently settles into a curve that shows a very weak Pe^* dependence.

Based on these results, we can say that there are two regimes of decay reflecting a cross-over between diffusion and advection dominated dynamics. This cross-over is further elucidated when we look at the shape of the *slowest decaying eigenmodes*. The exponential decay of the standard deviation is the signature of a so-called eigenmode solution of the differential equation. An eigenmode $\rho_i(r, \varphi)$ is defined by the property

$$(-\mathrm{Pe}\, \boldsymbol{u} \cdot \nabla + \nabla^2)\rho_i = \mu_i \rho_i. \tag{4.11}$$

For each eigenmode ρ_i there is therefore a corresponding solution of the advection-diffusion equation that takes the form

$$\begin{aligned} \partial_t(\rho_i e^{\mu_i t}) &= \mu_i \rho_i e^{\mu_i t} \\ &= \left(-\mathrm{Pe}\, \boldsymbol{u} \cdot \nabla + +\nabla^2\right) \rho_i e^{\mu_i t} \\ &= \mu_i \rho_i e^{\mu_i t} . \end{aligned} \tag{4.12}$$

In other words, if a profile ρ_i is an eigenmode of the advection-diffusion equation, its shape will remain constant in time and its time evolution will take the form of an exponentially decreasing amplitude. The rate of decay is determined by the so-called *eigenvalue* μ_i. If a solution has a number of eigenmode components

$$\rho = \sum_i A_i \rho_i e^{\mu_i t} , \tag{4.13}$$

then these eigenmodes will decay at different rates μ_i. After some time, the decay will then be determined by the slowest decaying eigenmode, since all other amplitudes will have become negligible. In the case of the advection-diffusion equation, the asymptotic state $\rho_0 = 1$ is in fact an eigenmode, which is a bit special in the sense that its eigenvalue $\mu_0 = 0$. At long times the concentration is then approximated by

$$\rho \simeq 1 + A_1 \rho_1 e^{\mu_1 t} + \text{h.o.t.} . \tag{4.14}$$

The time evolution of $\sigma(\rho)$ should therefore be given by:

$$\sigma(\rho) \simeq A_1 \sigma(\rho_1) e^{\mu_1 t}. \tag{4.15}$$

We can therefore determine μ_1 by fitting an exponential to the tail of the $\sigma(\rho)$ curves, after which ρ_1 can be approximated by

$$\rho_1 \simeq (\rho - 1) e^{-\mu_1 t}\,, \tag{4.16}$$

which we average over the tail of the curve.

Figure 4.4 shows eigenmodes obtained with this method for Pe = 50 – 2000, corresponding to $\mathrm{Pe}^* = 3.7 - 150$. The corresponding eigenvalues are shown in figure 4.3c. At first glance, the eigenmode profiles are qualitatively similar to the transient profiles in figure 4.1. At low Pe^* the mode ρ_1 shows a single minimum that shifts towards the centrifugal zone as the strength of the transverse flow increases. However, a key difference becomes visible around $\mathrm{Pe}^* = 37$, where an increasingly pronounced tongue develops that ultimately leads to a form of bifurcation, where the single minimum on the centrifugal side splits into two minima located at the centres of the two circulation loops.

The slowest decaying mode thus shows a transition between two asymptotic shapes. At low Pe^* the profile approaches its symmetric diffusive form. At high Pe^* the asymptotic shape of ρ_1 thus converges a concentration profile that resembles the shape of the stream-function ψ. Since both asymptotic forms depend only weakly on the Péclet number, this explains the apparent transition in the decay rate visible in figures 4.3(a-b).

It therefore appears that there is something like a 'sweet spot' in the range of Péclet numbers, where the dependence on the flow strength is strongest. We can visualise the bifurcation in ρ_1 by looking at the degree of asymmetry in the profile. To do so we decompose ρ into its even and odd constituent terms:

$$\begin{aligned} \rho &= \rho^{\text{even}} + \rho^{\text{odd}}\,, \\ &= \sum_{n\ \text{even}} \rho^n \cos(n\varphi) + \sum_{n\ \text{odd}} \rho^n \cos(n\varphi)\,. \end{aligned} \tag{4.17}$$

For the terms that are odd in n, $\rho(r, \varphi_+) = -\rho(r, \varphi_-)$, whereas for even terms $\rho(r, \varphi_+) = \rho(r, \varphi_-)$. The magnitude of the odd modes thus determines the degree of asymmetry of the concentration profile around the $x = 0$ line. We can quantify the degree of symmetry by separating the amplitudes $\sigma(\rho_1^{\text{even}})$ and $\sigma(\rho_1^{\text{odd}})$ of the slowest decaying mode. A plot

of the asymmetry (fig 4.3) reveals a well-defined peak over the range of Péclet numbers where the bifurcation takes place with a maximum around $\mathrm{Pe}^* = 10$.

What these results show is that the helicity of the flow can in fact enhance diffusive flux into and out of the vacuole. The extent of this enhancement is determined by the eigenvalue μ_1 of the slowest decaying mode, since it the determines the rate of change of the concentration. Moreover, it appears that there is something like an optimum Péclet number in terms of the benefit that can be derived in terms of enhancing the flux.

The exact physiological implications of this effect remain difficult to pinpoint. The dependence of μ_1 on the Péclet number is moderate, implying a flux increase of roughly 25% at $\mathrm{Pe}^* = 10$. At $\lambda = 12$, a typical wavelength value at the peak of cell development, this would correspond to a Pe value of about 1200, which would mean this effect could be relevant for larger proteins with a diffusion constant around 20 $\mu\mathrm{m}^2/\mathrm{s}$. Whilst the vacuole is known to contain a variety of salts, photoassimilates and other small molecules, it is not known whether protein-sized objects are contained in the vacuole, and whether their diffusion rates are physiologically pertinent. For small molecules, which have a diffusion constant around 1000 $\mu\mathrm{m}^2/\mathrm{s}$, the the transverse Péclet number should be expected to be of order $\mathrm{Pe}^* \simeq 0.2$, which is too small to be significant.

So while we have clearly established that the helical flow in the vacuole provides a mechanism by which diffusive exchange may be sped up, it remains to be seen whether these effects are strong enough to provide a significant benefit to the organism. Of course, in this particular problem we have chosen the symmetry in such a way that the downstream component of flow does not factor in to the problem. In the next section we will assess how streaming affects transport along the length of the cell.

4.2 Homogenisation of Downstream Transport

In the previous sections we have looked at the role of the transverse circulation in enhancing fluxes into and out of the vacuole. In order to quantify the role of vorticity in downstream transport, a different kind of metric is required. A well known phenomenon relating to diffusive dispersion in a shear flow is *Taylor diffusion* (Taylor, 1953), classically discussed in the context of a the parabolic shear profile that is found for a pressure driven flow in a pipe. If a shear flow is seeded with a sheet of solute at $z = 0$, this

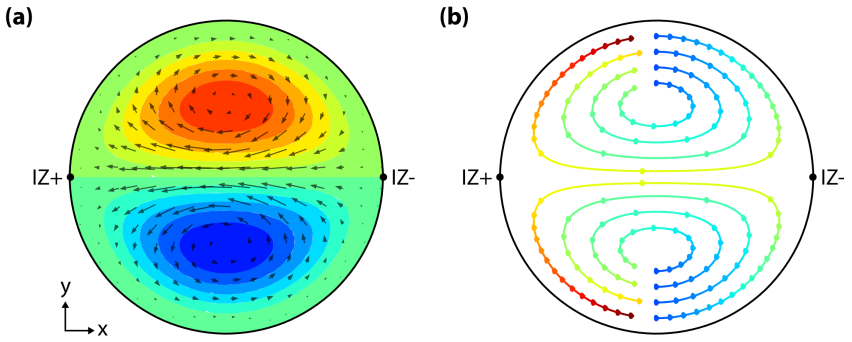

Figure 4.5 Poincaré mapping of downstream advection. **(a)** Stream function ψ at $\lambda = 3$ with corresponding circulation components of flow. (b) Poincaré plot of a set of trajectories. The line indicates the (r, φ) coordinates of a fluid element as it is advected, with colours indicating displacement along the z-axis, and markers indicating a z-displacement of $\lambda/4$. At $\lambda = 3$, trajectory lengths at the positions shown vary between 3-8 helical wavelengths.

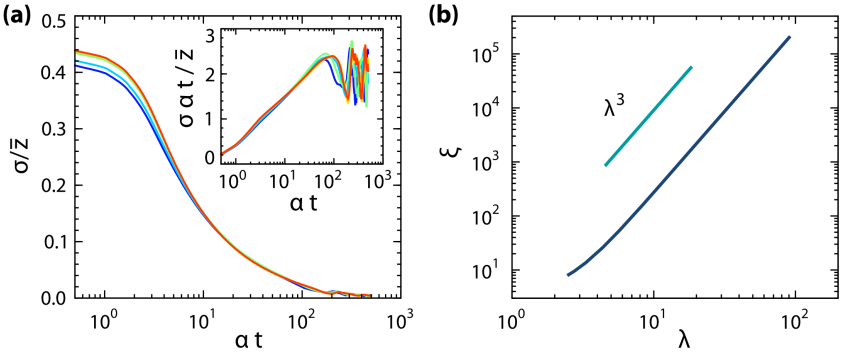

Figure 4.6 Homogenization of downstream transport. (a) Relative standard deviation of z-displacements tends to zero in a time $\propto 1/\alpha$ due to logarithmic growth of the absolute standard deviation (*inset*). Curves of different colours show a collapse of datasets with $\lambda = 3.0, 5.7, 12, 25, 47$. (b) The length ξ over which the z-displacements homogenize scales as $\mu z_i/\alpha$, showing a λ^3 dependence as the circulation decreases to zero.

sheet will undergo a parabolic deformation due to the shear flow. This will induce a radial concentration gradient, causing outward diffusion at the tip of the parabolic profile and inward diffusion at the tail. On time scales long enough for the solute to redistribute radially by diffusion (i.e. $t \gg$ Pe) this will result in a self-similar concentration profile moving at the mean

velocity and spreading longitudinally with an effective diffusivity $\sim Pe^2$. This phenomenon persists in the presence of transverse circulation, which results in a lowered effective diffusivity (Erdogan and Chatwin, 1967) and shorter time scale for convergence to the Taylor dispersion limit, as in the case of the staggered herringbone micromixer (Stroock et al., 2002).

The Taylor diffusion approximation will not necessarily hold for the comparatively short characean internodal cells, whose aspect ratio ($\sim 10^2$) implies that the longitudinal advection time L/V is comparable to the radial diffusion time R^2/D:

$$\frac{T_D}{T_A} = \frac{R^2}{D}\frac{V}{L} = \mathrm{Pe}\frac{R}{L} \sim 1\,. \tag{4.18}$$

However, even on these intermediate time scales, z-displacements are homogenized to some extent as fluid parcels are advected along vortex loops in the $r\varphi$-plane. Figure 4.5 shows the stream-function at $\lambda = 3$ along with a Poincaré plot of the $r\varphi$-coordinates of integrated trajectories. The colours denote the total distance travelled along the z-axis, with the markers indicating intervals of $\lambda/4$. On any given stream-line, fluid parcels advected by the flow travel roughly the same distance along the z axis as long as we wait long enough for the particles to traverse on full loop in the $r\varphi$-plane. On average, these fluid trajectories will then have moved along the z-axis at roughly the velocity at the centre of the circulation loop. The length of the plotted trajectories varies between 3-8 helical wavelengths. So if we seed the $z = 0$ plane with a sheet of points and compute their advective trajectories, we should expect the dispersion of the z-displacements to level off over several helical wavelengths, thus 'homogenising' the rate of transport along the z-axis.

To quantify this homogenisation we numerically compute the time-dependent variation in z-displacements for a set of points homogeneously distributed the $z = 0$ plane. Figure 4.6a shows the standard deviation $\sigma(z_i)$ of trajectory z-coordinates, normalised by their mean $\overline{z_i}$. As expected this relative variation decreases with a typical time that is wavelength dependent. However the curse for $\lambda = 3.0, 5.7, 12, 25, 47$ collapse when the time is rescaled by $\sim 1/\alpha_\psi$ indicating that the determining parameter is once again the strength of the transverse flow. The absolute magnitude of $\sigma(z_i)$ (Fig. 4.6a, inset) shows a logarithmic dependence that levels off as the grid resolution of the trajectories becomes insufficient to continuously represent the diverging circulation time at the wall.

With these results it becomes possible to calculate a typical loop time τ_ψ over which $\sigma(z_i)/\overline{z_i}$ falls off to half its initial value, as well as a corresponding length of transport is $\xi = \tau_\psi \overline{z_i}$ over which z-displacements homogenize. The dependence of ξ on λ (fig 4.6b) is dominated by a $1/\alpha_\psi$ dependence, leading to a very strong λ^3 scaling as the amplitude of the stream function approaches zero.

4.3 Helicity in Relation to Cell Development

Summarising the work above, we see that we have identified two ways the helicity of streaming could affect transport and mixing in the vacuole. One is that transverse circulation affects the rate of diffusive flux into and out of the vacuole by changing the typical size of the boundary layer at the periphery. The second is that the circulation helps homogenise downstream transport rate by advecting slowly moving material in the centre towards faster moving regions near the wall.

Since in both cases this effect depends on the magnitude of the transverse circulation α_ψ, it is worthwhile to examine what data exists regarding the helical pitch during development. We have in fact found one study that presents measurements of the helicity of characean internodes. In a set of experiments published in 1954, Paul Green measured the spiral wavelength of a *Nitella* cell over a week of growth (Green, 1954). The results from his experiments are reproduced in figure 4.7. A noticeable minimum in the wavelength occurs during the early days of growth (fig 4.7b – middle panel), as has been metioned anecdotally elsewhere (Green and Chapman, 1955). Given our analysis, we now realise that a decrease in wavelength means an increase in the vacuolar circulation as parametrised by the amplitude α_ψ of the stream-function.

The bottom panel shows the dimensionless growth rate of the surface area $(\partial S/\partial t)/S$, calculated from a spline interpolation of the datapoints for L and R. The resulting curve bears out the notion that the peak in growth rate coincides with the minimum in helical wavelength λ. At the height of development $\alpha_\psi = 0.014$, indicating that $\mathrm{Pe}^* > 1$ for $D < 100\ \mu\mathrm{m}^2/\mathrm{s}$, showing that the effects described in this chapter could just about be relevant for some more slowly diffusing molecules and proteins. While the observed effects are on the lower bound of what could still be significant, Green's data does seem to suggest that a cell may derive benefit by increasing its helical pitch during growth to enhance intracellular transport rates.

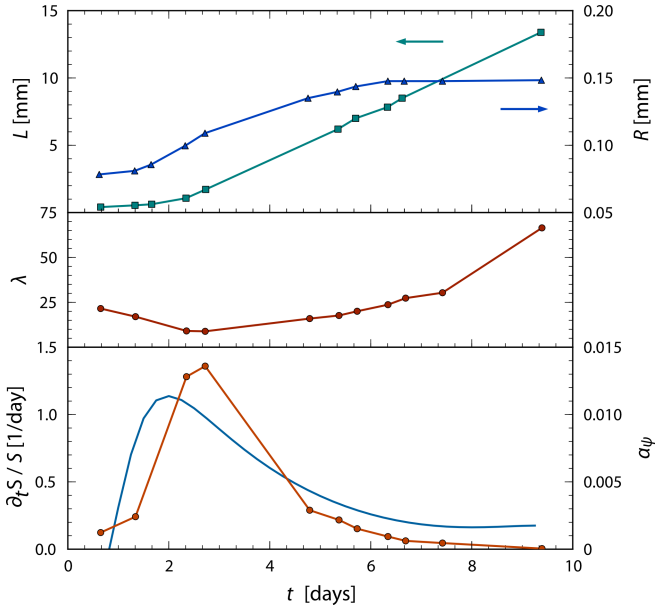

Figure 4.7 Comparison with experiments from Green (1954). (top panel) Cell length L and radius R and (middle panel) helical wavelength λ as measured by Green. (bottom panel) Corresponding amplitude of transverse flow α_ψ, as compared with cell dimensionless growth-rate calculated from spline interpolation of the measured dimensions.

Summary

In this chapter we have sought to quantify how the transverse circulation in characean internodes might aid transport and mixing in the vacuole. We have found two mechanisms by which the transport might benefit from this circulation.

The first is revealed when looking at the response to a change in concentration at the periphery. During re-equilibration a boundary layer forms at the periphery, whose typical length scale δ is determined by the strength of the outward flow at the centrifugal neutral zone. A scaling law $\delta \sim \mathrm{Pe}^{*-1/3}$ is observed for the boundary layer size, which can be explained by a standard dominant balance argument near the indifferent zone. Once the boundary layer has developed, the tail of the re-equilibration process is dominated by the slowest decaying eigenmode ρ_1 of the equations. This mode shows a minimum that shifts towards the centrifugal neutral line as Pe^* is increased, which bifurcates into a state with two minima at the

centres of the circulation loops. Away from this bifurcation point, the ρ_1 mode shows a weak dependence on Pe^* as it converges to its $\mathrm{Pe}^* = 0$ and $\mathrm{Pe}^* = \infty$ asymptotic forms. The range of Péclet numbers for which a significant dependence is observed is therefore something like $\mathrm{Pe}^* = 1 - 100$. Over this range, the typical rate of flux, as determined by the eigenvalue μ_1 of the slowest decaying mode, increases roughly by a factor two.

The second mechanism we have studied is the influence of transverse circulation on downstream transport on intermediate time scales, where diffusion may be neglected. Here we observe the slightly counter-intuitive phenomenon that streaming actually helps homogenise the rate of transport along the z-axis. Since slowly moving material is eventually advected into faster moving regions by the transverse circulation, displacements will converge to the same average over a time scale that is of the order of the time required to traverse one loop in the $r\varphi$ plane. Further analysis shows that the ξ over which the transport rate homogenises shows a strong λ^3 dependence. For short wavelengths λ, this length ξ is order $100\,R$, which is a fairly typical length for a mature cell.

One big question regarding both these analyses is whether the transverse flows observed in vivo are in fact strong enough to be physiologically relevant. One problem in assessing this question is that the choice of Péclet number depends on the metabolite studied. A replotting of the measurements by (Green, 1954) shows that cell wavelength can vary from $9 - 70$ over the course of cell development. At its peak, the strength of transverse flow is about 1.4% of the velocity at the wall, suggesting that circulation could become relevant for solutes with a diffusion constant $D < 100\ \mu\mathrm{m}^2/\mathrm{s}$, which suggests that the helicity of the flow may aid transport processes for protein sized objects in the vacuole.